Velocity Temporal Shape Affects Simulated Flow in Left Coronary Arteries

Justen R. Geddes[1][0000−0001−6614−331X], Cyrus Tanade[1][0000−0002−2395−6908], William Ladd[1], Nusrat Sadia Khan[1], and Amanda Randles[1][0000−0001−6318−3885]

Duke University, Durham NC, 27708, USA
justen.geddes@duke.edu

Abstract. Monitoring disease development in the coronary arteries, which supply blood to the heart, is crucial and can be assessed via hemodynamic metrics. While these metrics are known to depend on the inlet velocity, the effects of changes in the time-dependent inlet flow profile are not understood. In this study, we seek to quantify the effects of modulating temporal arterial waveforms to understand the effects of hemodynamic metrics. We expand on previous work that identified the minimum number of points of interest needed to characterize a left coronary artery inlet waveform. We vary these points of interest and quantify the effects on commonly used hemodynamic metrics such as wall shear stress, oscillatory shear index, and relative residence time. To simulate we use 1D Navier-Stokes and 3D lattice Boltzmann simulation approaches conducted on high performance compute clusters. The results allow us to observe which parts of the waveform are most susceptible to perturbations, and therefore also to measurement error. The impacts of this work include clinical insight as to which portions of velocity waveforms are most susceptible to measurement error, the construction of a method that can be applied to other fluid simulations with pulsatile inlet conditions, and the ability to distinguish the vital parts of a pulsatile inlet condition for computational fluid dynamic simulations.

Keywords: Computational Fluid Dynamics · Coronary Arteries · Temporal Velocity Profile

1 Introduction

Coronary arteries supply blood to the heart and are vital to healthy human function. When these arteries narrow, a condition known as coronary artery disease (CAD), they impede blood flow, posing a significant health risk. Therefore, the ability to monitor and predict the future of CAD is a crucial challenge. CAD and other diseases have been shown to correlate with hemodynamic metrics such as wall stress [13]. Therefore, gaining insights into the factors influencing hemodynamic metrics is vital for comprehending disease progression. Specifically, the temporal inlet velocity profile is a key determinant of these hemodynamic metrics in the vascular system.

As with all measurements, the field should seek to quantify the effects of error in measurements such as the inlet velocity to understand their impact on both observed physiological states and simulations. In particular, state-of-the-art devices for measuring flow velocity, such as Doppler echocardiography, are prone to significant errors [7]. To understand these errors in the temporal domain, we study the effects of inlet velocity perturbations in computational fluid dynamics (CFD) simulations of the left coronary arteries as a proof of concept.

Previous works have successfully conducted pulsatile CFD in the left coronary arteries using a template waveform [2,19,23,24], while others use additional models, usually ordinary differential equations, to inform the coronary inlet from heart flow [5, 8, 11, 16, 22]. However, none of these studies considered perturbations or error in their inlet velocities. Rizzini et al. [18] quantified differences in inlet flow in the spatial development profile of the flow, but did not assess the temporal profile. Jiang et al. [9] studied the velocities of a temporal waveform by modulating a temporal waveform's minimum, average, and maximum velocities in the right coronary arteries. However, by only varying these general measurements of the profile, they were unable to quantify how differences in specific portions of the waveform can affect hemodynamics.

To our knowledge, no study has evaluated perturbations in the temporal shape of the inlet velocity of the left coronary artery or attempted to quantify the contributions of changes in specific parts of hemodynamic waveforms in general. Addressing this gap in the literature will allow for a better understanding of the impact of inlet conditions on hemodynamic metrics, measurement error of devices such as Doppler echocardiograms, and which portions of the inlet waveform are most important to hemodynamic metrics.

To accomplish this task, we use novel techniques from our previous study [6] to systematically stretch the inlet waveform to assess the effects of perturbations of portions of the inlet waveform. We simulate using 1D and 3D CFD approaches, thus allowing us to sample more plentifully with the low computational cost of 1D approaches, while also using 3D simulations to ensure the accuracy of simulations. We hypothesize that perturbation locations on the inlet waveform will not all produce the same effect on output metrics and that some points will be more important than others to capture accurate measurement and CFD results. Implications include the use of a non-uniform error tolerance in practice and identifying regions of increased interest when examining a patient's inlet velocity profile.

2   Methods

To assess the effect of waveform shape on hemodynamic metrics, we first choose the points that we wish to modulate to change the shape of the waveform. We then define our 1D and 3D models, as well as our geometries and numerical experiments. Lastly, we present the metrics that we use to characterize the hemodynamics.

2.1   Quantifying and varying temporal waveform shape

To assess how different waveform shapes modulate hemodynamic metrics, we must first specify how we will vary the shape of the waveform. To accomplish this task, we expand on our previous study [6] that used a novel "stretching" procedure to vary waveforms. This pipeline was applied to left coronary arteries and started with 20 possible points of interest (shown in Fig. 1) that could be stretched to change the shape of the waveform. The way these points are calculated is shown in Table 1. We denote the velocity value of point i as f_i and the time value of point i as t_i. Using this notation, our previous study found that the points t_5, t_6, f_4, f_5, f_6 and f_9 can well represent the variations in the waveforms. reducing points.
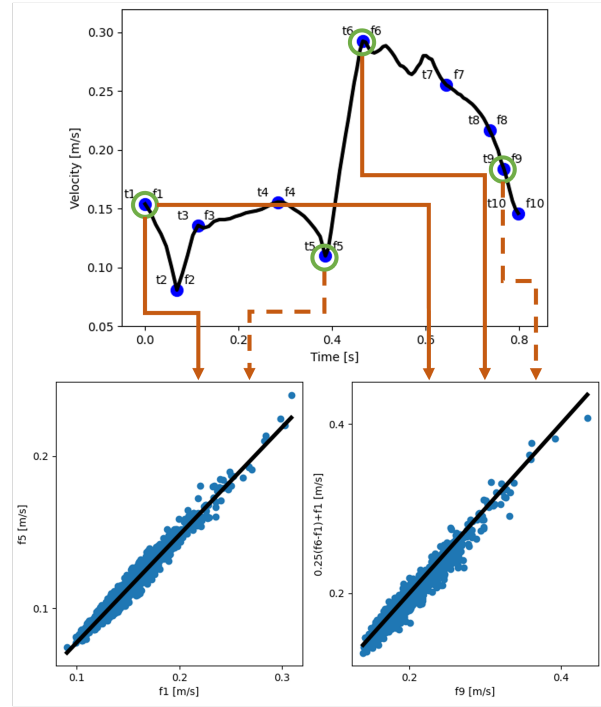
Fig. 1. Estimating points f_5 as a function of f_1 (bottom left) and f_9 as a function of f_1 and f_6 (bottom right). The top panel shows the points used to estimate, marked by solid arrows, and the points that are being estimated, marked by dashed arrows. The lower two panels show the linear relationship between the point and their estimators.

In the current study, our goal is to assess the effects of changing the first velocity point by vertically shifting the entire waveform, achieved by adding f_1 to the collection of points. Furthermore, we include the systolic valley for physiological significance (f_2).

Table 1. Definition of point locations on waveforms. Note that f_i refers to the velocity of point i. The location of all points can be seen in Fig. 1.

Point number	Description	Point number	Description
1	Beginning of systole	6	Diastolic peak
2	Systolic valley	7	$3/4\ (f_6 - f_{10}) + f_{10}$
3	Systolic shoulder	8	$1/2\ (f_6 - f_{10}) + f_{10}$
4	Systolic max	9	$1/4\ (f_6 - f_{10}) + f_{10}$
5	Beginning of diastole	10	End of cardiac cycle

Additionally, note that $f_9 = 0.25(f_6 - f_{10}) + f_{10}$. We observe that the first and last points are approximately equal ($f_1 \approx f_{10}$), and therefore $f_9 \approx 0.25(f_6 - f_1) + f_1$, and estimate f_9 as such. Lastly, we observe a strong ($R^2 = 0.97$) linear correlation between f_1 and f_5, and therefore estimate f_5 as $f_5 \approx 0.70797f_1 + 0.00665$. These relations are depicted in Fig. 1.

Finally, we have our set of points to modify: $s = \{t_5, t_6, f_1, f_2, f_4, f_6\}$, while using the modified values to estimate f_5 and f_9 to preserve physiological waveform shape while "stretching". These points are depicted in Fig. 2.
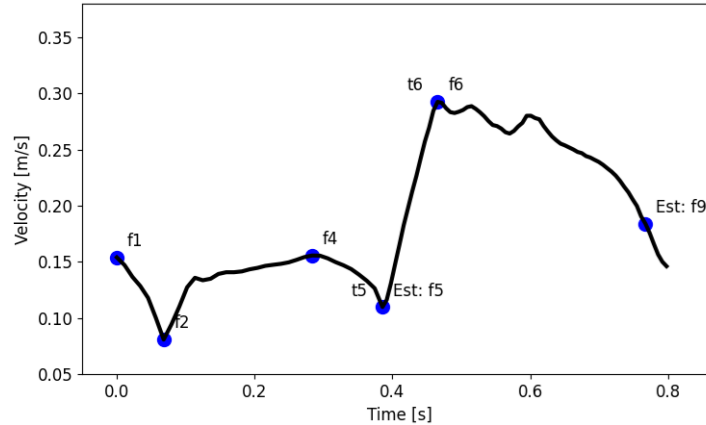
Fig. 2. The final selected points on a left coronary artery inlet velocity waveform. "Est" denotes points that are estimated using the values of other points, but are not independently modulated.

2.2   1D simulation approach

One-dimensional blood flow was simulated using the methods outlined in [3, 4, 20, 21] which are based on the equations

$$\frac{\partial A}{\partial t} + \frac{\partial Q}{\partial x} = 0 \tag{1}$$

$$\frac{\partial Q}{\partial t} + \frac{\partial}{\partial t}\left(\alpha\frac{Q^2}{A}\right) + \frac{A}{\rho}\frac{\partial P}{\partial x} = -C_f\frac{Q}{A} \tag{2}$$

where Q is the flow rate [m^3/s], t is time [s], A is cross-sectional area [m^2], α modulates the velocity profile, x is the spatial position [m], $\rho = 1{,}060$ kg/m^3 is the density of blood, P is pressure [Pa], and $C_f = 22\pi\mu$ (where μ is the dynamic viscosity [Pa s]) introduces effects from friction. P relates to A via

$$P = P_{\text{ext}} + \beta(\sqrt{A} - \sqrt{A_0}), \beta = \frac{\sqrt{\pi}hE}{(1-\nu^2)A_0} \tag{3}$$

with P_{ext} denoting external pressure on the vessel and A_0 cross-sectional area under no pressure. β represents vessel stiffness and is computed using wall thickness, h, elastic modulus, E, and Poisson's ratio (ν). We use values from [20].

Boundary conditions were enforced using a 2-element Windkessel model to represent the effects of flow in the microvasculature as

$$Q = \frac{P}{R} + C\frac{dP}{dt} \tag{4}$$

with C [m^3/Pa] denoting compliance and R [(Pa s) / m^3] denoting resistance.

2.3   3D simulation approach

To simulate 3-dimensional blood flow, we use our in-house parallel fluid solver, HARVEY [17]. HARVEY uses the lattice Boltzmann method, which is a mesoscopic approach shown to recover the Navier-Stokes equations, to represent the fluid as a collection of particles that are quantified via particle distribution functions [12]. These distribution functions change in time and space per the lattice Boltzmann equation,

$$f_i(x + c_i\Delta t, t + \Delta t) = f_i(x,t) + \Omega_i(x,t), \tag{5}$$

with x denoting the spatial position, t representing time, c_i is a discrete velocity, and Ω_i is the Bhatnagar–Gross–Krook collision operator. HARVEY utilizes the D3Q19 velocity discretization with finite difference boundary conditions at inlets and outlets [14] as well as the halfway bounce-back condition, which enforces the no-slip condition at the rigid walls.

### 2.4   Image-derived Coronary Geometries

It is critical to examine realistic geometries to assess waveform variation. We use image-derived 3D geometries reconstructed from 2D coronary angiograms by the methods described in [1]. This study was approved by the Duke University Medical Center Institutional Review Board (Pro00091022) and limited data can be provided on request from the authors. To obtain a 1D geometry, we calculated the centerlines using Mimics [15]. Once centerlines were obtained, we used techniques presented in [4] to create an interconnected tree of 1D domains. In total, we examined nine different patient-specific left coronary artery geometries.

2.5   Numerical experimental protocol

In order to assess how differences in the shape of the inlet waveform affect hemodynamic metrics, we use patient-specific waveforms created by scaling the template waveform using cardiac output and heart rate. To assess the effect of shape on these waveforms we first calculate the average value of each of the six points, $\overline{s_i}$ ($s = \{t_5, t_6, f_1, f_2, f_4, f_6\}$) across the nine different geometries.

For the 3D predictions of blood flow, we simulated the patient-specific waveform and also one trial for each selected point with the waveform "stretched" to increase the chosen point by 10% of the average, i.e. s_i becomes $s_i + 0.1\overline{s_i}$. 10% is chosen to align with the approximate Doppler echocardiogram error tolerance [7, 10]. These modifications are illustrated in Fig. 3b. Thus, we conduct 7 simulations per geometry, 63 total.

The 1D model is much less computationally expensive than 3D, which allows for more simulations than 3D. On average, 3D simulations were run on 46 nodes and took between 4-12 hours, while 1D simulations take only a fraction of this time. For 1D simulations, for each geometry we simulate the patient-specific waveform, and then 40 simulations ranging from ±20% with one simulation for each percentage, e.g., point s_i becomes $s_i - 0.2\overline{s_i}$ for the -20% simulation. These trials are illustrated in Fig. 3a. We simulate ±20% for 1D simulations to cover the worst-case scenarios. Some waveforms were not physiological due to $t_5 > t_6$ or $t_5 \approx t_6$ and therefore were omitted. This protocol generates a maximum of 241 simulations per geometry (6 points of interest, up to 40 simulations per point of interest, and one baseline simulation), 2,169 simulations in total.
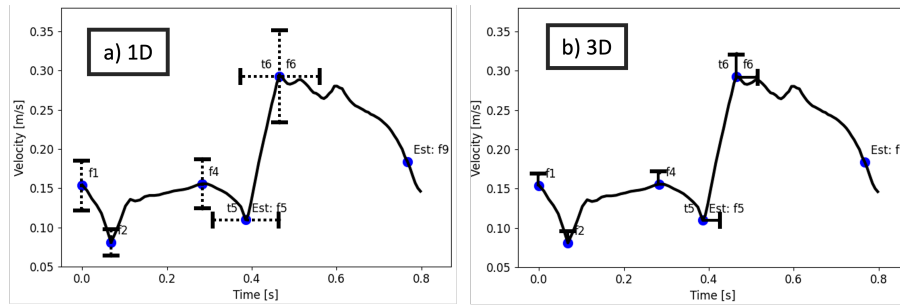
Fig. 3. How the waveforms were stretched in simulations. In panel a), the dashed lines denote 40 simulations were conducted between -20% of the average point value and +20%. panel b) shows the simulations for 3D simulations, with each solid bar denoting one simulation with the point increased by 10%.

2.6   Calculating Hemodynamic Metrics

For 1D simulations, we compute average and maximum wall shear stress (WSS) [Pa] over the geometry and the cardiac cycle, with WSS computed as

$$WSS = \frac{-4u\mu}{R} \tag{6}$$

with u [m/s] denoting the velocity at a particular spatial position, R [m] the radius of the vessel, and μ [Pa s] the dynamic viscosity of blood.

For 3D simulations, we calculate the maximum and average time-averaged wall shear stress (TAWSS) [Pa] over the geometry, with the TAWSS given by

$$TAWSS = \frac{1}{T} \int_0^T |\tau_w| dt \tag{7}$$

with T [s] denoting the time for a cardiac cycle and τ_w [Pa] the wall shear stress imposed by the moving fluid. To verify the results, we compare WSS (1D) and TAWSS (3D) for the same magnitude of perturbations.

We also compute the maximum and average oscillatory shear index (OSI) [N.D.] over the geometry, with OSI calculated as

$$OSI = 0.5 \left(1 - \frac{|\int_0^T \tau_w dt|}{\int_0^T |\tau_w| dt} \right) \tag{8}$$

which captures the effects of oscillatory flow on walls. In addition, we also calculate maximum and average relative residence time (RRT) [Pa^{-1}],

$$RRT = \frac{1}{(1 - 2\,OSI)\,TAWSS}. \tag{9}$$

We examine the relative difference of hemodynamic measurements as $r = (m_1 - m_0)/m_0$ where r is the relative difference [N.D.], m_1 is the metric computed from the perturbed waveform, and m_0 is the metric from the original patient-specific waveform.

2.7   Statistical Tests

We analyze the relative differences in two ways. First, we compare the output metric relative difference to the relative difference of the perturbation to observe whether the input perturbation is proportional to the output effects. These effects are denoted Fig. 4 and Fig. 5 as dashed lines. Secondly, we conduct an unpaired t-test with the null hypothesis of a mean equal to 0 for 3D simulations and that the slope of the line of best fit is equal to 0 for 1D simulations. We use a significance threshold of 0.005 for the unpaired t-tests.

3   Results

We first present results for 1D, followed by 3D, simulations. We then compared 1D and 3D results and, lastly, compared 3D results with inlet profile metrics.

3.1   1D Quantification of Wall Shear Stress

In our study, we conducted as many as 241 1D simulations for each geometry and show in Fig. 4 the 1D relative difference in maximum WSS and average WSS for each perturbed point compared to the original baseline simulation versus the percent change in the point of interest. The findings approximate a linear relationship, which allowed us to apply a linear regression analysis to the dataset. Subsequently, we compared the slopes of these lines to the null hypothesis that the slope is equal to 0.
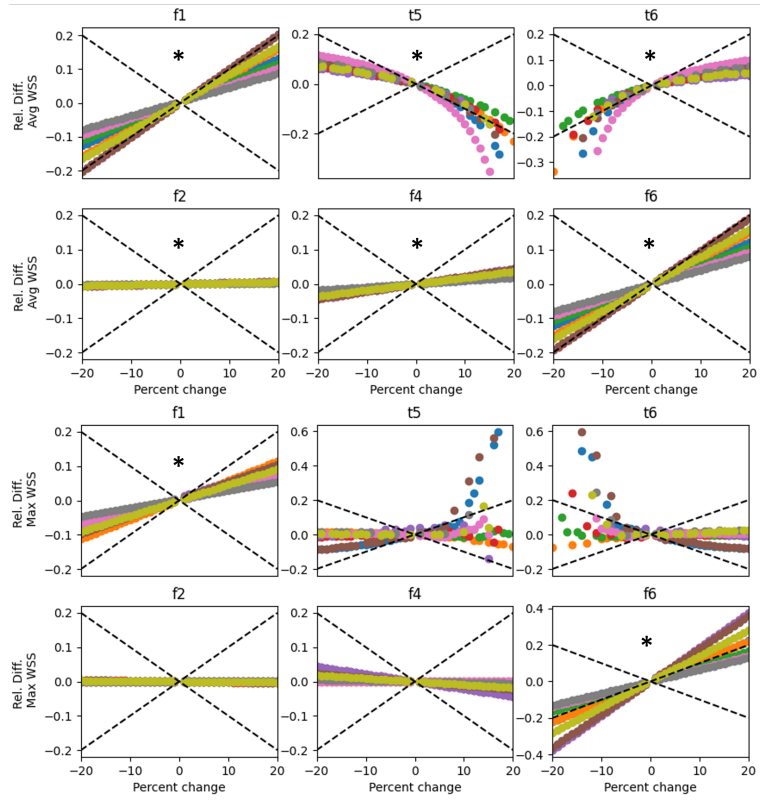
Fig. 4. Relative differences of average wall shear stress (WSS, top two rows) and maximum WSS (lower two rows) vs percent change of the point of interest for 1D simulations. Distinct geometries are noted by varying colors. Noting linear behavior, we compare the slope of the regression line of the line of best fit to a slope of 0, which implies no change due to varying the point of interest. A "∗" denotes a p-value < 0.005 using an unpaired t-test. Dashed lines denote a magnitude of change in the output metric equal to the magnitude of change in the point of interest ($y = x$).

We observe that all average WSS comparisons are significant ($p < 0.005$), as well as f_1 and f_6 maximum WSS. We further note that the changes in f_1 and f_6 are approximately equal to the change in the average WSS. Additionally, there is nonlinear behavior for t_5 and t_6 as they become closer to each other. Lastly, while f_2 and f_4 have statistically significant slopes, the change in the output metrics is minor compared to the amount of change in the point of interest.

3.2   A Subset of Perturbed Points of Interest resulted in Significant 3D Simulation changes

Since 3D simulations are more computationally expensive than 1D, we conducted only one simulation for each point of interest per geometry, increasing the point of interest by 10% of the average value of points in all geometries. Fig. 5 shows the results for TAWSS, OSI, and RRT. We observe that the average and maximum TAWSS are significant for each point of interest, with the largest effects observed for f_1 and t_5. Furthermore, the average OSI is significant for t_5, t_6, and f_2 while the average RRT is significant for f_1, f_4 and f_6.

3.3   Strong Agreement between 1D and 3D Wall Shear Stress

We use 1D simulations to explore the parameter space more widely than computationally expensive 3D simulations. However, viewing the 1D results as an extension of 3D requires that the 1D and 3D produce similar relative differences where they overlap – in WSS/TAWSS at a +10% perturbation. To verify this agreement, Fig. 6 shows the Bland-Altman plot between the relative differences in the 1D and 3D simulations where the points of interest were increased by 10% of the average value between the geometries. We see that there is good agreement between 1D and 3D, with a bias of 0.0033 [N.D.] and a standard deviation of 0.02 [N.D.]. We also observe that as the magnitude of 1D predictions increases, the difference between predictions increases, thus causing the points on the left of the figure. Lastly, we see that 3D TAWSS is usually larger than 1D WSS, thus causing most of the points to be less than zero.

3.4   Correlation between metrics and Inlet Waveform metrics

Given the above results, a natural question that follows is whether the calculated hemodynamic metrics can be predicted from the inlet waveform without simulation. Fig. 7 shows the comparison of TAWSS with the area under the temporal inlet velocity curve, the systolic area under the curve (AUC), diastolic AUC, systolic duration, cardiac cycle duration, average systolic velocity, average diastolic velocity, and average velocity. Each point represents a 3D simulation - one point for each trial per geometry, thus resulting in 63 points.

We observe that TAWSS is correlated with the average velocity and other metrics that would increase the average velocity. This correlation aligns with expectations, given that velocity is a central component of the TAWSS calculation.
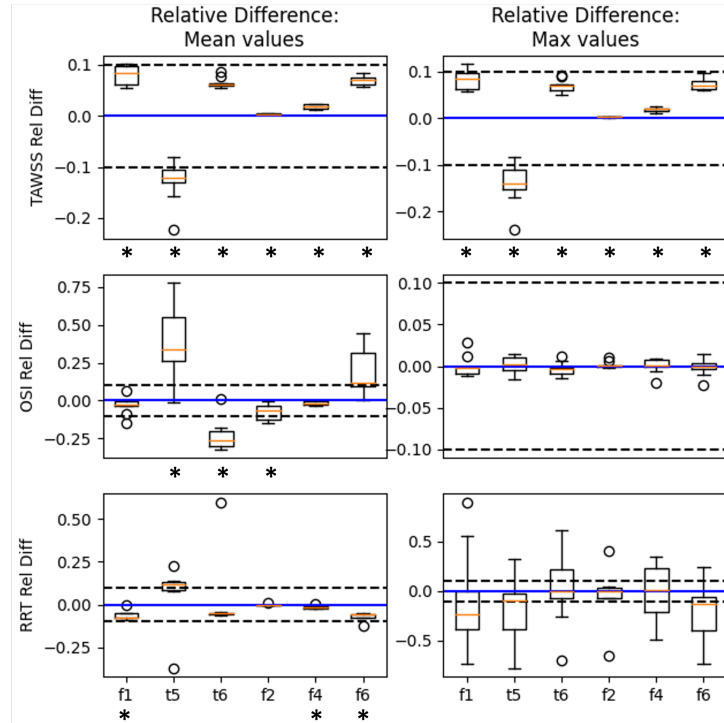
Fig. 5. 3D results for modulating points of interest by 10% of the average point value among geometries for time-averaged wall shear stress (TAWSS), oscillatory shear index (OSI), and relative residence time (RRT). Boxplots denote the distribution of 9 simulations, one for each geometry, for each point of interest. The solid blue line denotes the 0% change, while the dashed black lines mark $\pm$ 10% change. A "$*$" denotes a p-value < 0.005 using an unpaired t-test between the distribution and 0 (blue line), which would imply no output change for the perturbed point of interest.

We also detect a weak correlation with certain metrics like diastolic area under the curve (AUC), where we can identify distinct clusters of data points that are consistent across different perturbations and geometries. In contrast, we find no significant correlation between TAWSS and other metrics, such as systolic AUC or average systolic velocity. Additional results, which are not shown, indicate a lack of correlation between TAWSS and OSI or RRT.

4   Discussion

We explore the effects of alterations in the temporal profile of the coronary artery inlet velocity waveform on hemodynamic metrics, essential for tracking disease progression [13]. In particular, we elucidate which points of interest,
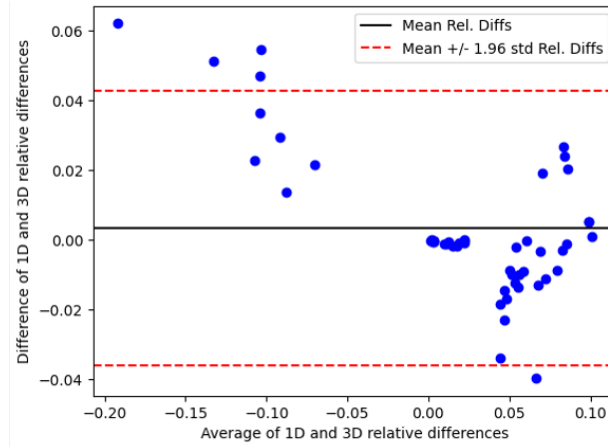
Fig. 6. Bland-Altman plot comparing 3D predicted time averaged wall shear stress (TAWSS) and 1D predicted wall shear stress (WSS). The solid black line denotes the mean of the difference between 1D and 3D, while the dashed red lines denote the mean ± 1.96 standard deviations.

which quantify the inlet waveform, are most sensitive to perturbations. We begin our discussion with 1D, and then 3D, simulation results and consider the relationship between the 1D and 3D results. Subsequently, we assert that relying solely on inlet waveform metrics is insufficient for precise predictions of hemodynamic metrics.

4.1   1D Linear Changes in Wall Shear Stress

Remarkably, perturbations of points of interest result in mostly linear changes in the 1D WSS. The exception to this linearity is when $0 < t_6 - t_5 \ll 1$. The linear change between point-of-interest perturbations and the relative change in WSS implies that changing point values does not greatly amplify input changes in point values, as would be suggested by an exponential relationship. Moreover, we see that the majority of the points result in relative differences of the output that are less than or equal to the relative differences of the input, as can be seen by the points in Fig. 4 being between the dashed black lines. This observation implies that the output effects are less than or equal to the corresponding input changes. Therefore, when considering how changing a waveform will affect the WSS of a new simulation, we can conclude that the WSS will change less than (or equal to) the change in the temporal waveform.

4.2   Three points of interest cause 3D statistically significant OSI differences

1D simulations are adequate to predict WSS, however, only 3D simulations can predict OSI and RRT. We see that in Fig. 5 that, as predicted by the 1D sim-
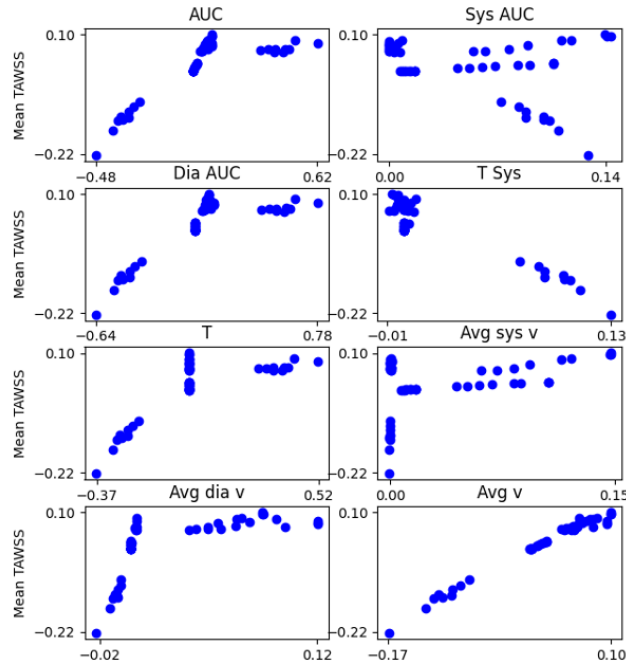
Fig. 7. Plots of the mean relative difference of perturbed simulation to original for TAWSS against relative differences for inlet waveform metrics: area under curve (AUC), systolic area under curve (sys AUC), diastolic area under curve (dia AUC), time for systole (T Sys), Cardiac cycle length (T), average systolic velocity (Avg sys v), average diastolic velocity (Avg dia v), and average velocity (v). Each color represents a distinct geometry.

ulations, the change in input is not amplified to the output (marked by dashed lines) in 3D simulations except for t_5. This amplification of the t_5 input arises because, by increasing t_5, we make $t_6 - 5_5 \approx 0$ as mentioned above.

It is expected and true that all TAWSS comparisons result in statistically significant differences since velocity is closely related to TAWSS. It is perhaps more interesting that t_5, t_6, and f_2 all affect the mean OSI differences. Furthermore, these differences represent sudden changes in velocity. This relation suggests that inlet velocity waveforms can have an effect on OSI and that OSI is not only geometry dependent. Additionally, we see that RRT is only statistically significant when OSI is not, likely because TAWSS is significant for all points and RRT is a function of TAWSS and OSI.

4.3   Inlet waveforms are not enough to predict all metrics

Given the above analysis, we wish to evaluate whether metrics that quantify the inlet velocity waveform can predict hemodynamic metrics without the need

to simulate. For OSI and RRT (results not shown), no inlet waveform correlated whatsoever with OSI or RRT. Additionally, the 1D WSS results displayed weak correlations. However, the average velocity in the 3D simulations was able to correlate well with the mean TAWSS (Fig. 7). Thus, in general, we require patient-specific modeling to quantify hemodynamic metrics.

4.4   Limitations

The presented work has limited 3D simulations due to the computational expense of the simulations. As a result, only seven 3D simulations were conducted for each of the nine geometries. We attempted to remedy this limited number of simulations by conducting up to 241 1D simulations. Furthermore, we only considered one template waveform for each geometry. As such, it is possible that these results could differ for other waveforms that, for example, are recorded in a hyperemic state.

4.5   Clinical and research implications

This work influences how waveforms are quantified in the clinic by measuring the effects of varying points of interest. Specifically, we see that the acceleration of flow may be most important to OSI, and that OSI depends on both geometry and inlet conditions. Additionally, we have shown that some points have a greater impact on hemodynamic metrics than others - such as peak diastolic velocity (f_6). Furthermore, while TAWSS can be estimated from inlet waveform measurements (such as average velocity), our findings advocate for the necessity of 1D and/or 3D simulations to accurately determine precise WSS, OSI, and RRT.

Lastly, the approximate linear behavior suggests that one could potentially predict the mean and maximum WSS for varying waves by simply simulating one wave of interest and quantifying how far points of interest on additional waves are from the original waves. Further work can apply this method to other portions of the vasculature.

5   Conclusion

The findings of our research underscore the critical influence of the waveform shape, beyond mean velocity, on key hemodynamic parameters such as WSS, TAWSS, OSI, and RRT. This nuanced understanding advances our capabilities in flow simulations of coronary hemodynamics, emphasizing the importance of time-domain inlet conditions. Furthermore, our work delineates the waveform segments most susceptible to inaccuracies and identifies the specific aspects of the temporal waveform that significantly impact hemodynamic metrics, offering vital insights for clinical assessments related to disease progression. This analysis was carried out in the left coronary arteries, but, as with the pipeline that precedes this work [6], can be generalized to other geometries. The impacts of this

work include an increased understanding of inlet conditions in CFD simulations, the identification of sensitive portions of the temporal waveform to error, and clinical insight as to which areas of the temporal waveform have the most effect on hemodynamic metrics and, therefore, also hold importance to disease states.

References

1. Chen, S.J., Carroll, J.D.: 3-d reconstruction of coronary arterial tree to optimize angiographic visualization. IEEE transactions on medical imaging **19**(4), 318–336 (2000)
2. Chidyagwai, S.G., Vardhan, M., Kaplan, M., Chamberlain, R., Barker, P., Randles, A.: Characterization of hemodynamics in anomalous aortic origin of coronary arteries using patient-specific modeling. Journal of Biomechanics **132**, 110919 (2022)
3. Feiger, B., Adebiyi, A., Randles, A.: Multiscale modeling of blood flow to assess neurological complications in patients supported by venoarterial extracorporeal membrane oxygenation. Computers in biology and medicine **129**, 104155 (2021)
4. Feiger, B., Kochar, A., Gounley, J., Bonadonna, D., Daneshmand, M., Randles, A.: Determining the impacts of venoarterial extracorporeal membrane oxygenation on cerebral oxygenation using a one-dimensional blood flow simulator. Journal of biomechanics **104**, 109707 (2020)
5. Fleeter, C.M., Geraci, G., Schiavazzi, D.E., Kahn, A.M., Marsden, A.L.: Multilevel and multifidelity uncertainty quantification for cardiovascular hemodynamics. Computer methods in applied mechanics and engineering **365**, 113030 (2020)
6. Geddes, J.R., Randles, A.: Optimizing temporal waveform analysis: A novel pipeline for efficient characterization of left coronary artery velocity profiles (2024), https://doi.org/10.48550/arXiv.2402.10146
7. Ghorbannia, A., Ellepola, C.D., Woods, R.K., Ibrahim, E.S.H., Maadooliat, M., Ramirez, H.M., LaDisa Jr, J.F.: Clinical, experimental, and computational validation of a new doppler-based index for coarctation severity assessment. Journal of the American Society of Echocardiography **35**(12), 1311–1321 (2022)
8. Gutierrez, N.G., Mathew, M., McCrindle, B.W., Tran, J.S., Kahn, A.M., Burns, J.C., Marsden, A.L.: Hemodynamic variables in aneurysms are associated with thrombotic risk in children with kawasaki disease. International journal of cardiology **281**, 15–21 (2019)
9. Jiang, Y., Zhang, J., Zhao, W.: Effects of the inlet conditions and blood models on accurate prediction of hemodynamics in the stented coronary arteries. AIP Advances **5**(5), 057109 (2015)
10. Kebed, K., Sun, D., Addetia, K., Mor-Avi, V., Markuzon, N., Lang, R.M.: Measurement errors in serial echocardiographic assessments of aortic valve stenosis severity. The international journal of cardiovascular imaging **36**, 471–479 (2020)

11. Kim, H.J., Vignon-Clementel, I., Coogan, J., Figueroa, C., Jansen, K., Taylor, C.: Patient-specific modeling of blood flow and pressure in human coronary arteries. Annals of biomedical engineering **38**, 3195–3209 (2010)

12. Krüger, T., Kusumaatmaja, H., Kuzmin, A., Shardt, O., Silva, G., Viggen, E.M.: The lattice boltzmann method. Springer International Publishing **10**(978-3), 4–15 (2017)

13. Kumar, A., Hung, O.Y., Piccinelli, M., Eshtehardi, P., Corban, M.T., Sternheim, D., Yang, B., Lefieux, A., Molony, D.S., Thompson, E.W., et al.: Low coronary wall shear stress is associated with severe endothelial dysfunction in patients with nonobstructive coronary artery disease. JACC: Cardiovascular Interventions **11**(20), 2072–2080 (2018)

14. Latt, J., Chopard, B., Malaspinas, O., Deville, M., Michler, A.: Straight velocity boundaries in the lattice boltzmann method. Physical Review E **77**(5), 056703 (2008)

15. Materialise: Mimics, https://www.materialise.com/en/healthcare/mimics-innovation-suite/mimics

16. Ramachandra, A.B., Kahn, A.M., Marsden, A.L.: Patient-specific simulations reveal significant differences in mechanical stimuli in venous and arterial coronary grafts. Journal of cardiovascular translational research **9**(4), 279–290 (2016)

17. Randles, A.P., Kale, V., Hammond, J., Gropp, W., Kaxiras, E.: Performance analysis of the lattice boltzmann model beyond navier-stokes. In: 2013 IEEE 27th International Symposium on Parallel and Distributed Processing. pp. 1063–1074. IEEE (2013)

18. Rizzini, M.L., Gallo, D., De Nisco, G., D'Ascenzo, F., Chiastra, C., Bocchino, P.P., Piroli, F., De Ferrari, G.M., Morbiducci, U.: Does the inflow velocity profile influence physiologically relevant flow patterns in computational hemodynamic models of left anterior descending coronary artery? Medical Engineering & Physics **82**, 58–69 (2020)

19. Sharma, P., Itu, L., Zheng, X., Kamen, A., Bernhardt, D., Suciu, C., Comaniciu, D.: A framework for personalization of coronary flow computations during rest and hyperemia. In: 2012 Annual International Conference of the IEEE Engineering in Medicine and Biology Society. pp. 6665–6668. IEEE (2012)

20. Tanade, C., Chen, S.J., Leopold, J.A., Randles, A.: Analysis identifying minimal governing parameters for clinically accurate in silico fractional flow reserve. Frontiers in Medical Technology **4**, 1034801 (2022)

21. Tanade, C., Feiger, B., Vardhan, M., Chen, S.J., Leopold, J.A., Randles, A.: Global sensitivity analysis for clinically validated 1d models of fractional flow reserve. In: 2021 43rd Annual International Conference of the IEEE Engineering in Medicine & Biology Society (EMBC). pp. 4395–4398. IEEE (2021)

22. Taylor, C.A., Fonte, T.A., Min, J.K.: Computational fluid dynamics applied to cardiac computed tomography for noninvasive quantification of fractional flow reserve: scientific basis. Journal of the American College of Cardiology **61**(22), 2233–2241 (2013)

23. Vardhan, M., Gounley, J., Chen, S.J., Chi, E.C., Kahn, A.M., Leopold, J.A., Randles, A.: Non-invasive characterization of complex coronary lesions. Scientific reports **11**(1), 1–15 (2021)

24. Vardhan, M., Gounley, J., Chen, S.J., Kahn, A.M., Leopold, J.A., Randles, A.: The importance of side branches in modeling 3d hemodynamics from angiograms for patients with coronary artery disease. Scientific reports **9**(1), 1–10 (2019)